Coupled Adsorption and Surface-Bound Radical-Mediated Oxidation on Biomass-Derived Porous Carbon: A Selective Approach for Sulfamethoxazole Removal

Yu Li [a, b], Jingdong Yang [a, b], Min Zhang [a, b], Zequn Yang [c], Kaimin Shih [d], Guang-Guo Ying [a, b], Yong Feng [a, b, *]

[a] SCNU Environmental Research Institute, Guangdong Provincial Key Laboratory of Chemical Pollution and Environmental Safety & MOE Key Laboratory of Theoretical Chemistry of Environment, South China Normal University, Guangzhou 510006, China

[b] School of Environment, South China Normal University, University Town, Guangzhou 510006, China

[c] School of Energy Science and Engineering, Central South University, Changsha 410083, China

[d] Department of Civil Engineering, The University of Hong Kong, Pok Fu Lam, Hong Kong, China

*** Corresponding author:**

Dr. Yong Feng

Phone: (+86) 020-84721549

Fax: (+86) 020-85213484

E-mail: fengy@scnu.edu.cn

ABSTRACT

The development of selective oxidation processes is significant for the efficient removal of organic micropollutants from aqueous streams. Here, we propose a novel catalytic system that involves highly efficient adsorption followed by surface radical-mediated oxidation via conjunction of biomass-derived porous carbon (BPC) and peroxydisulfate (PDS). A series of BPC samples were prepared via pyrolyzing biomass at different temperatures (600ºC, 700ºC, 800ºC). BPC800 had the best reactivity for sulfamethoxazole removal: The maximum adsorption capacity of BPC800 was 529.3 mg/g, which is more than four times that of activated carbon (125.4 mg/g). The co-presence of PDS changed the major removing mechanism from adsorption to degradation. Mechanistic studies using quenching tests, electrochemical characterization, and fluorescence microscopy showed that surface-bound radicals were the dominant reactive species. Efficient performance was also achieved during the treatment of real wastewater and several other micropollutants. The results suggest a novel approach for highly-efficient selective removal of micropollutants from polluted wastewater and offer new insights into the generation of reactive species during the activation of PDS by carbonaceous materials.

Keywords: Micropollutants; peroxydisulfate; porous carbon; sulfamethoxazole; surface-bound radicals

1. Introduction

Antibiotics are emerging contaminants and have aroused worldwide concern due to their broad presence in the environment with potential harm to human health [1, 2]. Advanced oxidation processes (AOPs) are a widely studied technology for the removal of antibiotics from water and wastewater via highly oxidative radicals, e.g., hydroxyl radicals (·OH) and sulfate radicals ($SO_4^{\cdot-}$). However, these radical species, particularly ·OH, are non-selective and short-lived (t ($SO_4^{\cdot-}$)$_{\text{half-lives}}$ = 30–40 μs, t (·OH)$_{\text{half-lives}}$ = 20 ns) [3]. Many common water constituents such as chloride ions (Cl^-; $k_{Cl^-,\cdot OH}$ = (4.2 ± 0.2) × 10^9 M^{-1} s^{-1}, $k_{Cl^-,SO_4^{\cdot-}}$ = 3.1 × 10^8 M^{-1} s^{-1}) [4, 5], bicarbonate ions (HCO_3^-; $k_{HCO_3^-,\cdot OH}$ = 8.5 × 10^6 M^{-1} s^{-1}, $k_{HCO_3^-,SO_4^{\cdot-}}$ = (9.1 ± 0.4) × 10^6 M^{-1} s^{-1}) [4, 6], and natural organic matters (NOMs, $k_{NOMs,\cdot OH}$ = (2.3 ± 0.77) × 10^4 L mgC^{-1} s^{-1}, $k_{NOMs,SO_4^{\cdot-}}$ = (1.53–3.50) × 10^3 L mgC^{-1} s^{-1}) [7, 8] react rapidly with these radicals and transform some of them to relatively lower oxidizing species. Antibiotics are micropollutants in natural water environments with typical concentrations of ng/L to μg/L [9]. These are one-thousandth the concentrations of the common water constituents mentioned above. Consequently, AOPs usually suffer from significant scavenging effects when used to remove micropollutants from real water matrices.

Selective oxidation processes are of great interest to environmental scientists because these technologies can effectively degrade target contaminants by greatly mitigating the scavenging effects of common anions and NOMs [10-12]. Of the several selective oxidation systems reported, the activation of persulfates using carbonaceous materials is highly promising with applications in practical water and wastewater remediation. As oxidant precursors, persulfates including peroxydisulfate (PDS) and

peroxymonosulfate (PMS) have remarkable merits such as easy activation, convenience in transport and storage, and a wide effective pH range [13-15]. Importantly, these oxidants can be activated in a nonradical way and have shown great effectiveness in the selective degradation of a variety of organic contaminants such as chlorophenols [16, 17], endocrine disruptors [3, 18], and sulfonamide antibiotics [19, 20]. The nonradical mechanism reported here via the activation of either PDS or PMS by carbonaceous materials generally includes singlet oxygen ($^1O_2$)-dominated oxidation [17, 21, 22] and catalyst (electron shuttle)-mediated indirect electron transfer (IET) [16, 23, 24]. Although $^1O_2$ was reported to have a high reactivity toward some electron-rich organic compounds, there is still a lack of direct evidence on the participation of $^1O_2$ in the degradation of contaminants. Water scavenges $^1O_2$ rapidly (2.5×10^5 s^{-1}) [25], and there is limited information currently available regarding the transformation of organic pollutants by $^1O_2$ (e.g., attacking mechanisms and degradation pathways). In the IET-mediated oxidation, electron-rich contaminants could be readily attacked, but the accumulation of the transformation products that lack electron-donating groups is a major concern.

Here, we propose a catalytic system to selectively remove emerging micropollutants from wastewater. This system involves highly efficient adsorption followed by surface radical-mediated oxidation via conjunction of biomass-derived porous carbon (BPC) and PDS. Biomass was used to prepare PC because of its obvious advantages, such as low cost, easy availability, and environmentally friendly nature. BPC could selectively adsorb micropollutants, and surface-bound radicals are comparable to free radicals in terms of oxidizing capability, but the former is more selective [33]. PC samples were prepared by pyrolyzing biomass at different temperatures followed by comprehensive

characterization.

The adsorption and catalytic reactivity of this BPC was investigated using sulfamethoxazole (SMX) and several other widely detected micropollutants as the target contaminants (Table S1). The reactive species and mechanisms for the activation and degradation were systematically explored using electron paramagnetic resonance, classical quenching tests, electrochemical analysis, fluorescence microscopy, and *in situ* spectroscopy. The contribution of surface radical-mediated oxidation was evaluated by conducting desorption experiments and exploring the transformation pathways of SMX. Finally, the selectivity and tolerance of BPC–PDS oxidation were evaluated by investigating the effects of common radical scavengers and purifying real wastewater.

2. Experimental Section

2.1 Chemicals and materials

All chemicals were reagent-grade and used as received. A complete list of chemicals is shown in Note S1. The effluent from Liede Wastewater Treatment Plant (WWTP, Guangzhou, China) was collected and used to test the potential matrices effect. The quality parameters are listed in Table S2.

2.2 Preparation of BPC and BC

A series of BPC were prepared by pyrolyzing waste coffee grounds at different temperatures (600°C, 700°C, and 800°C). The synthesized BPC samples with KOH activation were denoted as BPCx, where x represents the pyrolysis temperature. For comparison, the biomass-derived carbon material prepared via the pyrolysis of coffee

grounds at 800℃ without KOH activation was named BC. Detailed preparation steps are found in Note S2.

2.3 Characterization of carbonaceous materials

The materials were characterized by various surface-sensitive techniques with details in Note S3.

2.4 Adsorption and catalytic degradation

Unless specified, both the adsorption and catalytic experiments were conducted in 200-mL glass reactors at room temperature. A solution (100 mL) that contained 5 mg/L SMX and 0.5 mM PDS (for the catalytic experiments only) was transferred to the glass reactor, and its pH value was adjusted to the desired value with 0.1 M H_2SO_4 or 0.1 M NaOH. Carbonaceous material was added to the reactor to launch the adsorption or catalytic reaction. A magnetic stirrer (400 rpm) was used to keep the suspension of solids in the reactor. Aqueous samples (1 mL) were periodically withdrawn, filtered with 0.22-μm PTFE membranes, and mixed with excess sodium thiosulfate to terminate the further degradation of SMX (for the catalytic experiments only). Desorption experiments were conducted to quantify the contribution of catalytic oxidation; see details in Note S4.

2.5 Chemical analysis

SMX and the other selected pollutants were quantified by high-performance liquid chromatography (Agilent 1260 Infinity II) equipped with an Agilent Poroshell EC-C18 column (2.7 μm, 4.6 mm × 100 mm) and a DAD detector. Analytical details are listed in Table S3. The iodometric method was adopted to measure the residual PDS [34].

The total organic carbon (TOC) of water samples was monitored using a TOC analyzer (Shimadzu TOC-V CPH, Kyoto, Japan). Common inorganic anions including Cl^- and CO_3^{2-} were detected using a Dionex Aquion RFC ion chromatograph (Thermo Fisher) with an AS11-HC column (4 × 250 mm). The electrochemical experiments were performed on a CHI660E electrochemical workstation (CH Instruments, Shanghai, China) with a conventional three-electrode system (Note S5). The degradation products of SMX were analyzed using a Waters Acquity ultra-performance liquid chromatograph (UPLC) H-class system with a Xevo G2-XS triple quadrupole mass spectrometer (MS/MS). An Acquity UPLC BEH Shield RP C18 column (2.1 × 150 mm, 1.7 μm) was used for the separation. Detailed analytical conditions of UPLC and MS are listed Table S4 and Note S6, respectively.

Surface-bound radicals were characterized using fluorescence spectroscopy (PerkinElmer FL6500, UK) and fluorescence microscopy (Nikon ECLIPSE Ts2R, Japan) [33]. The 7-hydroxycoumarin (7-HC) was monitored as the marker of both free and surface-bound radicals, and coumarin was used as the radical probe. Details are described in Note S7 and Fig. S1.

3. Results and Discussion

3.1 Characterization of BPC and BC

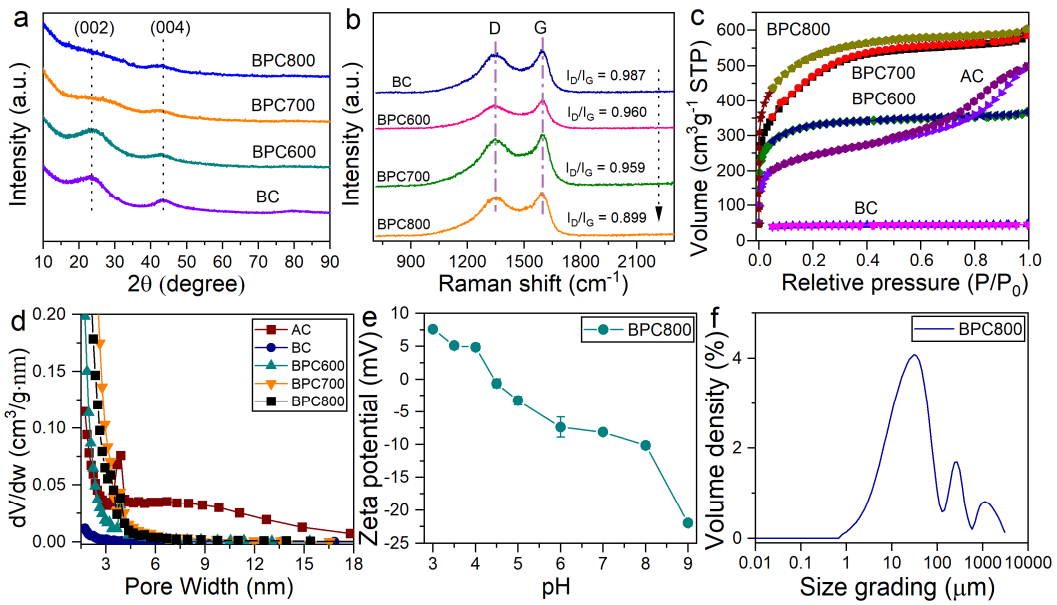

Figure 1. (a) XRD patterns, (b) Raman spectra, (c) N_2 sorption isotherms, (d) Barret-Joyner-Halenda (BJH) pore distribution, (e) zeta potential, and (f) particle size distribution of BPC.

The XRD diffraction patterns of different carbonaceous materials are shown in Fig. 1a. Two broad diffraction peaks at 23.4° and 43.2° were observed in the XRD patterns of BC and BPC600, and these peaks were indexed to the (0 0 2) and (0 0 4) planes of graphitic carbon. With increasing pyrolysis temperature, the diffraction peaks tend to be flat with an obviously decreased intensity: This suggests that the graphitization degree was significantly weakened, and the amorphous form was the dominant component in BPC, particularly in BPC800.

The Raman spectra of BC and BPC were investigated to further reveal the degree of graphitization (Fig. 1b). Two bands at a Raman shift 1350 and 1600 cm^{-1} were recorded and attributed to the characteristic D band (C atoms of defects or disordered structure) and G band (graphitic C structure), respectively. The intensity ratio of I_D/I_G is an

important parameter that reflects the defect degree in the structure of carbonaceous materials. These values were estimated to be 0.987, 0.960, 0.959, and 0.899 for BC, BPC600, BPC700, and BPC800, respectively, which suggests that the content of sp^2-hybridized carbon was increased with the enhanced pyrolysis temperature.

The N_2 sorption isotherms and specific surface area (SSA) are shown in Fig. 1c and Table 1, respectively; BC had the smallest SSA of 133.6 m^2/g. After activation using KOH, the SSA of BPC was greatly increased to 1041.5 m^2/g, and this value was greater than that of activated carbon (AC, 800.6 m^2/g). In addition, the pyrolysis temperature had a positive effect on the SSA of BPC; the SSA of BPC600, BPC700, and BPC800 was 1041.5, 1622.5, and 1704.8 m^2/g, respectively. Consistent with the SSA results, no obvious pores existed on the surface of BC (0.069 cm^3/g) (Fig. 1d and Table 1). After treatment using KOH, the total pore volumes of BPC were significantly increased from 0.069 to 0.913 cm^3/g. The zeta potentials of BPC at different pH values were measured (Fig. 1e). Positive potentials were recorded when the pH value was below 4.0, but the potential became negative when the pH was higher than 4.5. This suggests that the isoelectric point (pH_{iep}) of BPC was 4.0–4.5. In addition, particle size analysis showed that the diameter of most BPC800 in aqueous solution ranged from 1 to 100 μm (Fig. 1f).

Table 1. Physicochemical properties of carbonaceous materials.

Carbonaceous material	C (at%)	N (at%)	O (at%)	SSA (m^2/g)	Total pore volume (cm^3/g)	Average pore size (nm)
AC	89.7	0.6	9.7	800.6	0.726	3.63
BC	88.6	1.8	9.2	133.6	0.069	2.07
BPC600	92.1	1.9	5.7	1041.5	0.555	2.13
BPC700	92.5	2.5	4.7	1622.5	0.882	2.18
BPC800	92.4	0.7	6.7	1704.8	0.913	2.15

Data resource: XPS analysis and N_2 adsorption-desorption isotherm.

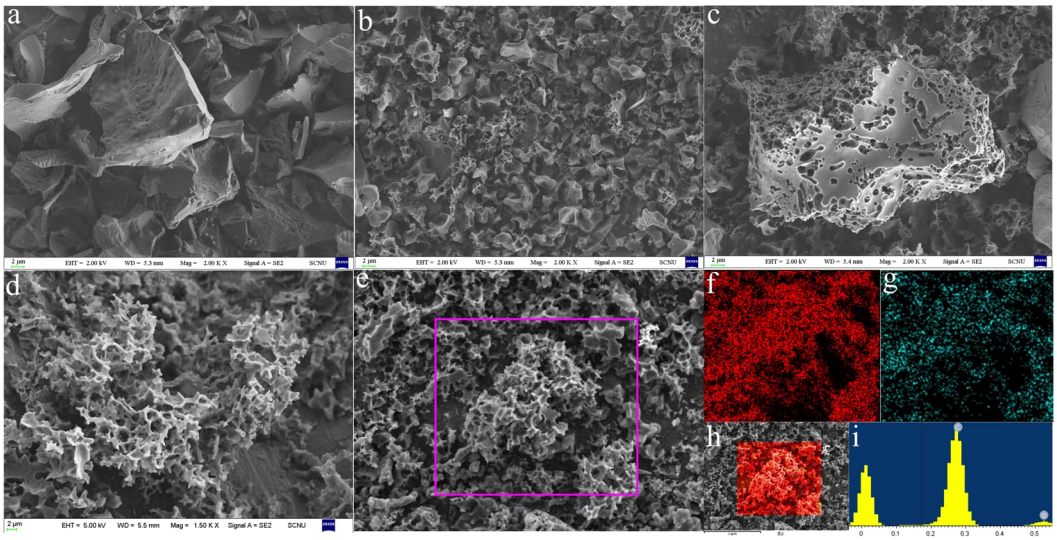

Figure 2. SEM images of (a) BC, (b) BPC600, (c) BPC700, and (d, e, h) BPC800; distribution of (f) C and (g) O elements in the area selected in (e); (i) EDS spectrum of the area selected in (h).

The morphology of the synthesized BPC samples was analyzed by scanning electron microscopy. BC had a smooth planar structure with no obvious pores (Fig. 2a). After activation with KOH, obvious porous structures were seen on the surface of all BPC samples (Figs. 2b–2d), which is consistent with the N_2 sorption results (Table 1) suggesting that the activation had a remarkable effect on the morphology of BPC. Pyrolysis temperature was found to influence the microstructure of BPC. A higher pyrolysis temperature implied the more intense pores on the surface of BPC (Figs. 2b–

2d). This observation is consistent with variations in the pore volume of different BPC samples. The elements on the surface of BPC were investigated by EDS. The C and O were distributed uniformly on the surface of BPC (Figs. 2f and 2g); these are the only elements that were detected by EDS (Fig. 2i).

3.2 Catalytic removal of SMX

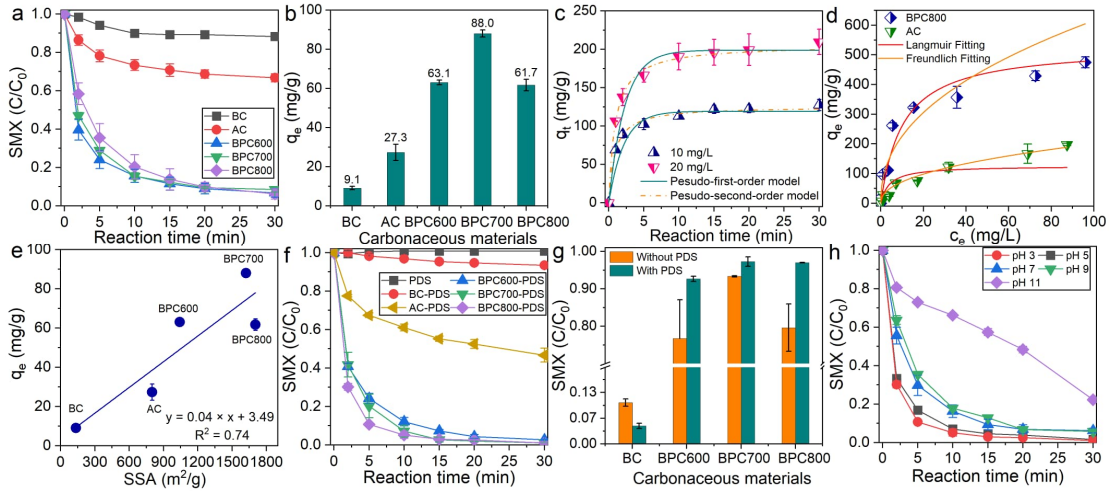

Figure 3. (a) Adsorption of SMX onto different carbonaceous materials in the absence of PDS; (b) absorption capacity of different carbonaceous materials toward SMX; (c) adsorption kinetics of SMX onto BPC800; (d) adsorption isotherms of SMX onto AC and BPC800; (e) correlation between q_e and SSA of different carbonaceous materials; (f) catalytic removal of SMX by PDS in the presence of different carbonaceous materials; (g) the removal of SMX with/without PDS; (h) effect of pH values on the catalytic removal of SMX by BPC800–PDS. Conditions: [SMX] = 5 mg/L, [PDS] = 0.5 mM, [carbonaceous materials] = 50 mg/L, and pH = 3.0.

The removal of SMX by different carbonaceous materials was also studied. Fewer than 12% of the SMX was removed by BC after reaction for 30 min (Fig. 3a), which suggests that BC had limited reactivity. However, an overall removal rate over 90% was achieved when BPC (BPC600, BPC700, BPC800) was used as the adsorbent. This removal rate was significantly greater than that achieved by AC (33.3%). After reaching equilibrium, the absorption capacities of BC, AC, BPC600, BPC700, and BPC800

toward SMX were 9.1, 27.3, 63.1, 88.0, and 61.7 mg/g (Fig. 3b), respectively. The adsorption capacities of BPCs were seven-fold greater than that of BC and more than twice that of AC, which demonstrates that BPC had much greater reactivity in the removal of SMX than the latter two adsorbents. This conclusion is consistent with the great difference in the SSA between BC and BPC—the larger pores after activation using KOH greatly improved the adsorption. However, the adsorption capacities of modified BPC samples at different pyrolysis temperatures for SMX were close to each other suggesting that the adsorption capacity was not only influenced by SSA and pore structure.

The kinetics for the removal of SMX was studies next. Equilibrium was reached within 15 min during the adsorption of SMX onto BPC (Fig. 3c). The pseudo-first-order law and pseudo-second-order law were used to model the adsorption of SMX (Note S8). As suggested by the fitting coefficients (R^2) (Table S5), the pseudo-first-order law and pseudo-second-order law performed equally well in modelling the adsorption of SMX onto BPC, which suggests that both chemisorption and physisorption contributed to the removal of SMX.

The Langmuir and Freundlich equations, two typical non-linear models, were selected to fit the experimental data (Note S8). The Freundlich model was more suitable than the Langmuir model for the adsorption of SMX onto AC (Fig. 3d and Table S6), thus implying that multilayer adsorption played a leading role. However, both models achieved identical good results when BPC was the adsorbent, which suggests that multilayer and monolayer adsorption co-existed during the adsorption of SMX onto BPC. The Langmuir isotherm indicates that the maximum adsorption capacities (q_{max},

mg/g) of BPC800 and AC for SMX were 529.34 and 125.36 mg/g (Table S6), respectively. q_{max} of BPC800 is more than four-fold that of AC. Physisorption is mainly influenced by the pore structure and SSA of adsorbents—a much greater adsorption capacity of BPC relative to BC underscores the role of physisorption. To further evaluate the contribution of physisorption, the relationship between SSA and its corresponding q_e was explored. A positive correlation ($R^2 = 0.74$) was observed among the prepared adsorbents (Fig. 3e), suggesting that physisorption was involved during the removal of SMX. However, the poor linear relationship and some mismatched data (for example, BPC800 with the largest SSA exhibited a lower adsorption capacity than BPC600) indicate that physisorption was not the only mechanism for the removal of SMX by BPC.

To improve the removal of SMX, the potential synergy between BPC and PDS was explored. PDS alone could not degrade SMX after reaction for 30 min (Fig. 3f); only 10% of the SMX was removed when BC was used to activate PDS. However, a remarkable increase in the removal of SMX was observed when BPC instead of BC and AC was co-present with PDS: Nearly complete removal of SMX was obtained within 15 min, and a removal rate of around 90% was achieved by BPC800–PDS after only 5 min of reaction. Except for the experiment with BC, the addition of PDS to the adsorption systems with BPC improved the removal of SMX (Fig. 3g), which reveals the synergy between PDS and BPC in the removal of SMX. The decrease in the removal rate of SMX by BC after the addition of PDS was probably due to the competitive adsorption on the surface of BC. Although AC could also activate PDS to degrade SMX, the removal kinetics of SMX by AC–PDS was significantly slower than that by BPC–PDS.

To comprehensively explore the catalytic reactivity of BPC, the removal of SMX by BPC800-PDS under different pH conditions (3–9) was investigated (Fig. 3h). As shown, the overall removal rate of SMX at all investigated pH values was 93.3–99.0% with only a slight decrease in the removal kinetics when the pH value increased in this range. However, there was a significant decrease in the catalytic removal of SMX when the pH was further increased to 11.0. The evolution of pH values during the removal of SMX by BPC800–PDS was monitored. After reaction for 10 min, the pH of the reaction media with initial pH values in the range of 3 to 9 was below the pK_{a2} of SMX (5.7) (Fig. S2), which suggests that SMX mainly presented in a neutral form in these reaction media. However, only a slight decrease in the pH value was observed when the initial value was 11.0. As the pH was much higher than the pK_{a2} of SMX, SMX was expected to present in a completely dissociated form. Meanwhile, BPC800 has a pH_{iep} value of 4.0–4.5 (Fig. 1e), and thus this material was also negatively charged at pH 11.0. Therefore, the decrease in the removal kinetics of SMX could be probably ascribed to the electrostatic repulsion between BPC800 and SMX.

To further reveal the relative contributions of adsorption and catalytic oxidation to the removal of SMX, desorption experiments were carried out and the amounts of SMX on the surface of reacted BPC800 were quantified. Around 76.0% and 5.6% of the SMX were present on the BPC800 after adsorption and catalytic degradation experiments (Fig. S3), respectively. The percentage of the SMX degraded by BPC800–PDS was estimated to be 83.8% after considering the recovery rate (~92%) and residual SMX in the reaction solutions. The reutilization capability of BPC800 was explored. Around 87.4% of the SMX could still be removed in the third consecutive catalytic cycle by

BPC800–PDS (Fig. S4), which suggests that BPC800 can be reused to activate PDS for contaminant degradation.

3.3 Activation and degradation mechanisms

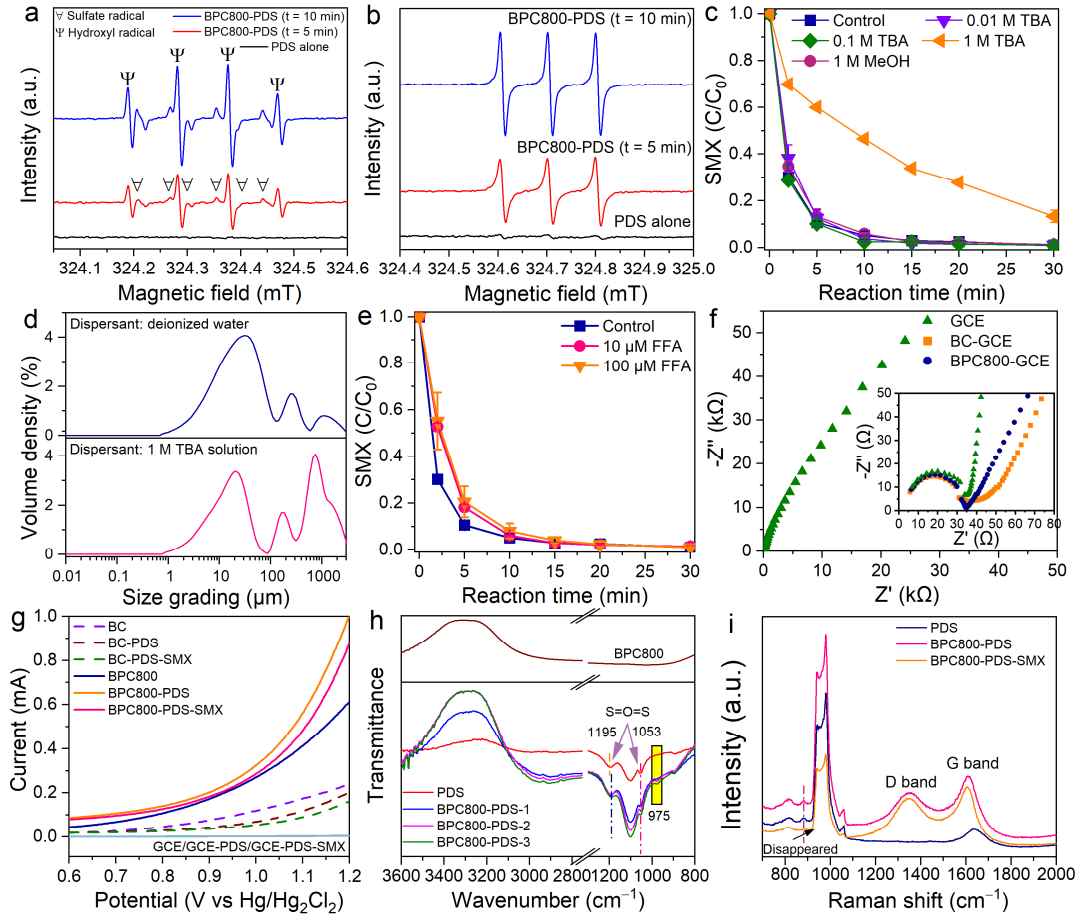

Figure 4. EPR spectra of BPC–PDS with (a) DMPO and (b) TEMP as the trapping agents; the effects of (c) MeOH, (c) TBA, and (e) FFA on the removal of SMX by BPC800–PDS; (d) effect of TBA on the size distribution of BPC800 in aqueous solutions; (f) AC impedance spectra (inside is a partially enlarged view) of BC and BPC800; (g) linear sweep voltammetry of different reaction systems; (h) ATR-FTIR spectra, and (i) Raman spectra of PDS, BPC800, and BPC800–PDS oxidation. Three parallel samples of BPC800–PDS oxidation were measured for the ATR-FTIR analysis. Conditions: [SMX] = 5 mg/L, [PDS] = 0.5 mM, [BPC800] = 50 mg/L, and pH = 3.0.

$SO_4^{\cdot-}$, ·OH, and $^1O_2$ are the typical reactive oxygen species (ROS) generated during the

activation of PDS. Therefore, EPR was used to explore the generation of these ROSs. Figs. 4a and 4b show no obvious signal when PDS existed alone. By contrast, the characteristic signals of DMPO-OH (Fig. 4a), DMPO-$SO_4^{\cdot-}$ (Fig. 4a), and TEMPO (Fig. 4b) were successfully recorded when BPC800 was co-present with PDS. These results suggest that the ROS including $SO_4^{\cdot-}$, ·OH, and $^1O_2$ were probably formed during the interaction between BPC800 and PDS. To assess the contribution of these ROS in the removal of SMX, quenching experiments using different alcohols including MeOH, TBA, and FFA were performed. These substances react actively with the ROS mentioned above (Table S7) and are widely used as scavengers in AOPs. Fig. 4c shows that MeOH with strong quenching ability for both $SO_4^{\cdot-}$ and ·OH had no obvious inhibition on the removal of SMX even though its concentration was as high as 1 M ([MeOH]/[SMX] = 50,000). TBA actively interacts with ·OH only and exhibited a similar negligible effect to MeOH when presented at relatively low concentrations (≤0.1 M). The absence of an inhibitory effect from both MeOH and TBA suggests that free radicals ($\cdot OH_f$, $SO_{4,f}^{\cdot-}$) were not involved during the removal of SMX by BPC800–PDS.

A significant suppression effect was observed when the concentration of TBA was increased to 1 M (Fig. 4c). TBA is a hydrophobic solvent, and the strong inhibitory effect of 1 M TBA was probably due to the reduced adsorption of SMX. On the one hand, the presence of TBA was expected to influence the partition behavior of SMX decrease its adsorption onto BPC800 (Note S9). On the other hand, TBA accelerated the aggregation of BPC800, which was detrimental to the adsorption of SMX. The removal of SMX in the presence of TBA was studied to verify this explanation. The removal rate of SMX by BPC800 with TBA was 21.3% lower than that without TBA

(Fig. S5). Meanwhile, significant aggregation of BPC800 was observed when TBA was present (Fig. S6). Furthermore, the size grading of BPC800 with the highest volume density in water changed from 30 to 750 μm after the addition of 1 M TBA (Fig. 4d). In addition to BPC, we investigated the behavior of a series of common AOP catalysts in the presence of TBA and similar phenomena were observed (Figs. S7 and S8). Besides MeOH and TBA, FFA with a concentration that was five times that of SMX had no obvious scavenging effect (Fig. 4e), which excludes the involvement of $^1O_2$ during the catalytic degradation. MeOH and TBA are hydrophilic radical scavengers and cannot quench surface-adsorbed radicals [37-39]. Considering that both $SO_4^{\cdot-}$ and ·OH were successfully recorded by EPR (Fig. 4a), these ROS were probably in surface-bound states ($SO_{4,s}^{\cdot-}$, $\cdot OH_s$) and oxidized the SMX that was pre-adsorbed to the surface of BPC800.

In addition to scavenging tests, we also studied the contribution of catalyst-mediated indirect electron transfer (IET). Here, a metastable complex between the catalyst and persulfate forms and withdraws electrons from the organic pollutant [23]. IET is a common pathway proposed for the nonradical degradation of pollutants by carbonaceous material-activated persulfates—particularly PDS [16, 40, 41]. BPC has abundant functional groups, large specific surface area, and strong electron conductivity. It is readily available as an electron shuttle to facilitate IET. To evaluate the conductivity of the prepared materials, the electrochemical impedance spectroscopy (EIS) of BC and BPC800 was measured (Fig. 4f). Compared to a bare glassy carbon electrode (GCE) with excellent conductivity, the Nyquist plots of BC and BPC800 have smaller semicircle diameters in the high frequency region, suggesting that both BC and BPC800 had a lower impedance and had faster electron transfer than GCE. The

diameters of the Nyquist plots of BC and BPC800 were almost identical indicating that the activation with KOH had only a slight effect on the conductivity of these samples.

Linear sweep voltammetry was used to investigate the electron transfer process (Fig. 4g). When bare GCE was used as the working electrode, there was no apparent current response before or after the addition of PDS or SMX, thus suggesting that there was no electron transfer in the GCE–PDS–SMX system. A weak current (~0.23 mA) was observed when GCE was modified with BC (BC/GCE electrode). However, the current was decreased when PDS and SMX were added, which indicates that electron transfer was also absent in the BC–PDS–SMX system. The BPC800/GCE had a higher current (~0.61 mA) than BC/GCE. Meanwhile, the addition of PDS increased the current, thus suggesting that electron transfer existed between BPC and PDS, and a complex ([BPC–PDS]*) probably formed [20, 24]. The adsorption of BPC800 toward PDS was seen by the significant removal of PDS by BPC800 alone and the strong competitive adsorption effect of SMX. Around 68.0% of the PDS was removed after interacting with BPC800 for 30 min, and the overall removal rate of PDS was decreased to 45.6% when 50 mg/L SMX was added (Fig. S9).

ATR-FTIR spectra were recorded to further study the interaction between BPC and PDS (Fig. 4h). Versus BPC800 alone, the spectra of BPC800–PDS showed adsorption peaks at 1195, 1053, and 1100 cm^{-1}, corresponding to the symmetric and asymmetric vibrations of S=O=S in the sulfonate group as well as S–O stretching vibration [24, 42, 43], respectively. In the presence of BPC800, a slight redshift of 7 cm^{-1} in the symmetric peak was observed, which indicates that the electron density of S=O=S was weakened due to the bonding effects between BPC800 and PDS [44]. Moreover, a new

peak located at 975 cm^{-1} emerged in the BPC800–PDS system, which suggests the formation of [BPC–PDS]* complex.

If there was electron transfer between [BPC–PDS]* and SMX, then the addition of the latter substance was expected to increase the current intensity. However, the presence of SMX decreased the current intensity instead (Fig. 4g), which indicates that there was no electron transfer between [BPC–PDS]* and SMX. Rather, direct electron transfer (DET) between BPC and PDS in [BPC–PDS]* probably occurred and generated $SO_{4,s}^{\cdot-}$ and $\cdot OH_s$. In the IET-mediated persulfate activation, the metastable complexes formed between activators and persulfate could be recorded by Raman spectrometry [45]. In this study, no such complexes were observed in the Raman spectrum (Fig. 4i), which is attributed to the presence of DET, which made [BPC–PDS]* much less stable. Meanwhile, the Raman analysis showed that the decomposition of PDS was enhanced by the addition of SMX (Fig. 4i), which explains the slight acceleration in the removal of PDS by BPC800 when 5 mg/L SMX was present (Fig. S9). In addition, the characteristic triple signal of TEMPO (Fig. 4b) could probably be attributed to the electrophilic attack of [BPC–PDS]* toward TEMP. In such reactions, TEMP lost an electron to form $TEMP^{\cdot+}$, which reacted with dissolved molecular oxygen to generate TEMPO [16, 46, 47].

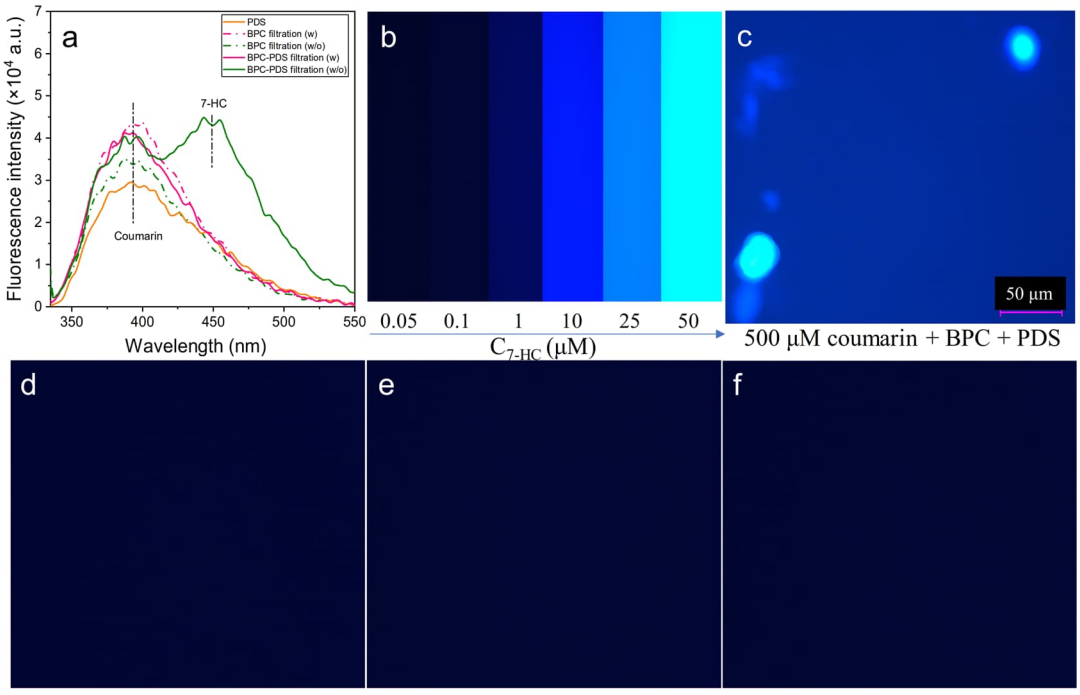

Figure 5. (a) Generation of 7-HC in different reaction systems; (b) colorimetric references of 7-HC solutions (0.05–50 μM), and (c–f) fluorescence microscopy images of the coumarin solutions after being exposed to different reaction systems. Conditions: [PDS] = 0.5 mM, [BPC800] = 100 mg/L, [coumarin] = 500 μM, and pH = 3.0.

Fluorescence analysis was used to understand the surface-bound radicals. Here, 7-HC was only generated when PDS and BPC800 were simultaneously present (Fig. 5a). No 7-HC was detected when the sample withdrawn from the BPC800–PDS system was filtered before mixing with the coumarin solution. These observations consistently suggest that radicals were formed and are presented on the surface of BPC800. As shown in Fig. 5b, 7-HC solutions of 0.1–50 μM are visually discernible. Fluorescence microscopy images of the coumarin solutions after being exposed to different reaction systems were recorded. The fluorescence microscopy images of BPC800-coumarin or PDS-coumarin were similar to coumarin alone (Figs. 5c–5e), thus suggesting that no 7-HC was formed. When BPC800 and PDS were co-present, the surface of BPC800 was a cyan color, and the color changed sharply to blue in the solid–liquid interphase and

bulk solution (Fig. 5f). These data suggest that high levels of radicals were formed and are presented on the surface of BPC800. These surface radicals resulted in the formation of 7-HC by reacting with coumarin.

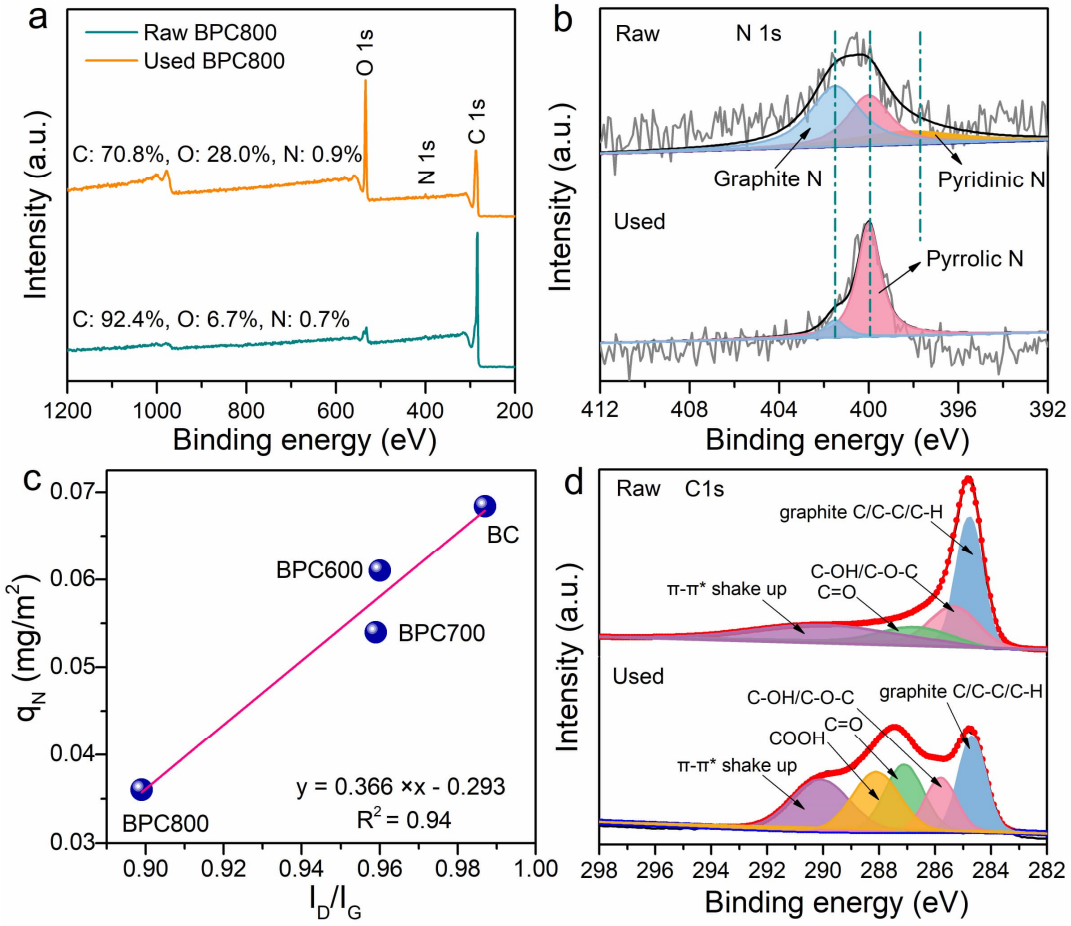

Figure 6. (a) XPS survey spectra, high-resolution (b) N 1s, and (d) C 1s XPS spectra of raw and used BPC800; (c) correlation between I_D/I_G and q_N of different carbonaceous materials.

Both adsorption and catalytic degradation ($SO_{4,s}^{\cdot-}$, $^{\cdot}OH_s$) contributed to the removal of SMX and the adsorption involves physisorption and chemisorption. However, the adsorption mechanism, particularly regarding the active site for chemisorption, is still unknown. Therefore, the XPS spectra of BPC800 before and after the reaction were investigated. Compared with raw BPC800, the N content of used BPC800 increased from 0.70% to 0.99% (Fig. S10a), suggesting that SMX was exactly adsorbed onto the

458 surface of BPC800. Moreover, the content of C–OH functional group after the
459 adsorption decreased by 1.22% (Fig. S10b), which indicates that the C–OH may act as
460 active sites for SMX adsorption. As for BPC800-PDS system, the full-scan XPS spectra
461 show that the surface composition of BPC800 changed during the reaction, and the
462 proportion of O content increased remarkably from 6.7% to 28.0% (Fig. 6a).
463 Meanwhile, N on the fresh BPC800 was detected with an atomic ratio of 0.72% and
464 consisted of pyridinic, pyrrolic, and graphitic N with percentage ratios of 28.3%, 31.5%,
465 and 40.2% (Fig. 6b), respectively. After the activation reaction, pyridinic N disappeared
466 and the percentages of pyrrolic and graphitic N changed to 87.5% and 12.5%,
467 respectively. Pyrrolic N could act as an electron donor to combine with organic
468 substrates (electron accepter) via an "donor–accepter complex" mechanism [29, 49].
469 Therefore, pyrrolic N was a chemisorption site and formed "donor–accepter complexes"
470 with SMX. To exclude the influence of surface area, the adsorption capacity was
471 normalized by SSA and defined as q_N (Table S8). Fig. 6c shows the good linear
472 relationship (R^2 = 0.94) between I_D/I_G and q_N of different biochar samples, thus
473 indicating that the defect sites or amorphous carbon might also play an important role
474 in the chemisorption of SMX.
475
476 Here, the C 1s XPS spectrum of pristine BPC800 was fitted into four groups including
477 C=C/C−C/C−H, C−OH/C−O−C, C=O, and a π–π* mixture (Fig. 6d) (Table 2). The C
478 1s XPS spectrum of used BPC800 changed significantly after the catalytic reaction. The
479 spectrum was divided into five groups including C=C/C−C/C−H, C−OH/C−O−C, C=O,
480 COOH, and π-π* mixture. As shown by their percentages, COOH was newly formed
481 during the catalytic reaction and both C=C/C−C/C−H and C−OH/C−O−C were
482 transferred to the other groups. Carbonyl groups (C=O) might disturb the conjugated π

system due to its strong electron-withdrawing ability, while hydroxyl groups (C−OH) as an electron-donating group could reinforce the electron density of the conjugated π system [50]. Therefore, the C−OH groups are likely the major active sites for PDS adsorption and activation while C=O had a limited contribution. Upon consumption of these active sites, the catalytic reactivity of BPC800 gradually decreased, which explains the slight decline in the removal of SMX over consecutive catalytic cycles (Fig. S4). To further confirm the presence of C−OH groups on BPC800, Boehm titration and FTIR analysis were performed (Note S10). Abundant acidic sites including phenolic, lactone, and carboxylic were detected on the surface of BPCs (Table S10). In all BPCs, phenolic groups were the leading acidic site, which indicates that numerous C–OH groups were situated on BPCs. On the contrary, no basic site was detected. Meanwhile, two broad peaks at the wavenumbers of 3600–3800 and 1450–1600 cm^{-1} were observed (Fig. S11), which correspond to the bonded O–H and C=C groups, respectively. These results verify the presence of C–OH groups.

$$BPC-OH + S_2O_8^{2-} \rightarrow [BPC-HO-S_2O_8^{2-}]\ ([BPC-PDS]^*) \quad (1)$$

$$[BPC-HO-S_2O_8^{2-}] \xrightarrow{DET} BPC-O^{\cdot} + SO_{4,s}^{\cdot-} + SO_4^{2-} + H^+ \quad (2)$$

$$SO_{4,s}^{\cdot-} + H_2O/OH^- \rightarrow \cdot OH_s + SO_4^{2-} \quad (3)$$

Based on the discussion above, a tentative mechanism was proposed for the activation PDS and degradation of SMX (Fig. 7). First, SMX and PDS were adsorbed onto the surface of BPC800 via both physisorption and chemisorption. Second, the adsorbed PDS interacted with the surface functional groups of BPC800 (e.g., C−OH) and formed a complex ([BPC–PDS]*) (Eq. 1). Third, DET within the [BPC–PDS]* complex instead of the IET between [BPC–PDS]* and SMX occurred to generate $SO_{4,s}^{\cdot-}$ (Eq. 2), which then interacted with the H_2O ($\leq 5 \times 10^2\ s^{-1}$) [51] and OH^- ($4.6 \times 10^7\ M^{-1}\ s^{-1}$) [4] on the surface of BPC800 to form $\cdot OH_s$ (Eq. 3). Finally, the resulting ROS attacked the

adsorbed SMX and degraded this contaminant.

Table 2. Surface functional groups of raw and used BPC800.

C 1s	Binding energy (eV)	Raw (%)	Used (%)
Graphite C/C−C/C−H	284.8	39.66	20.70
C−OH/C−O−C	285.3	22.09	13.36
C=O	286.7	13.12	20.46
π-π*	290.0	25.13	23.44
COOH	288.1	0	22.04

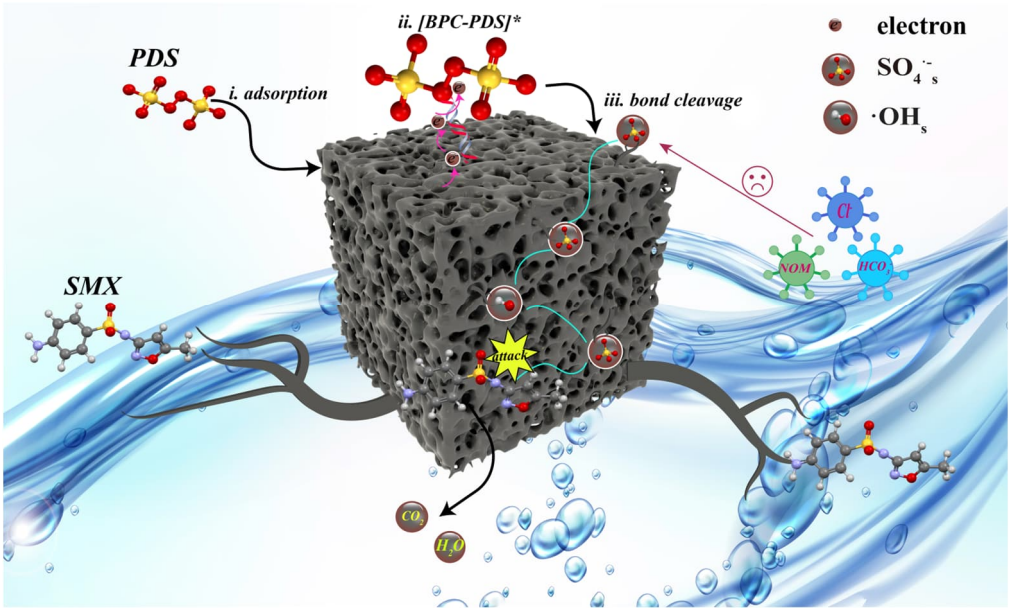

Figure 7. Proposed mechanisms for the removal of SMX by BPC800–PDS oxidation.

To clarify the fate of degraded SMX, its transformation products (TP) were identified using UPLC-MS/MS. Nine intermediates from TP1 to TP9 were detected (Table S11). On the basis of these TPs, four pathways were proposed for the degradation of SMX (Fig. 8). The electron-rich nature of SMX facilitated electrophilic reaction. In pathway 1, the amine group on the benzene ring was attacked by $SO_{4,S}^{\cdot-}$ and $\cdot OH_S$, which generated TP1 (Figs. S12 and S13). The nitroso group in TP1 readily interacted with radicals to form TP2 (Fig. S14) [52, 53]. The N–S bond in TP2 easily cleaved under the attack of radicals [54, 55], thus generating TP3 (Fig. S15) and TP4 (Fig. S15). Similarly,

522 the electrophilic addition of C=C bond on the isoxazole ring also occurred in the
523 presence of $\cdot OH_s$, thus leading to the formation of M-1 [56]. Although M-1 was not
524 detected, the successful detection of TP5 (Fig. S16) suggests that this compound was
525 involved during the degradation of SMX (pathway 2). The hydroxylation of the
526 isoxazole ring rendered it more susceptible to cleavage, thus leading to the formation
527 of isoxazole ring-opening products [57].
528
529 Here, similar isoxazole ring-opening products including TP5, TP6 (Fig. S17), and TP7
530 (Fig. S18) were also detected. The possible explanation was that the N–O bond on the
531 isoxazole ring in M-1 was attacked, and a methyl group was released, which led to the
532 formation of the carboxyl group in TP5. Subsequently, the carboxyl group in TP5 was
533 released followed by electron rearrangement, finally resulting in the aldehyde moiety
534 in TP6. The aldehyde moiety in TP6 was released under further radical attack, which
535 produced TP7. Pathway 2 was consistent Guan et al. [58].
536
537 In pathway 3, the C1 in the structure of SMX was attacked by $\cdot OH_s$ leading to the
538 formation of TP8 (Fig. S19) [59]. Moreover, the C–N (C3–N7) bond could also cleave
539 under radical attack [60]. The detection of TP9 (Fig. S20) confirmed the cleavage of
540 the C–N bond (pathway 4). Unfortunately, another bond-broken intermediate (M-2)
541 was not found, which might be attributed its unstable nature in the presence of highly
542 oxidizing species.

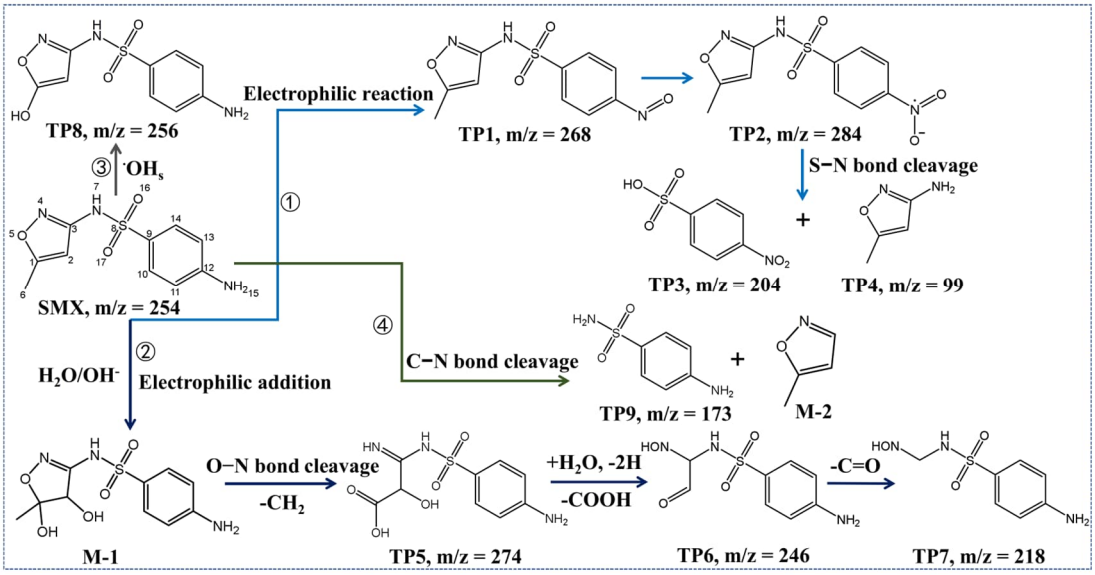

Figure 8. Proposed pathways for the degradation of SMX by BPC800–PDS oxidation.

3.4 Effects of water matrices and applications

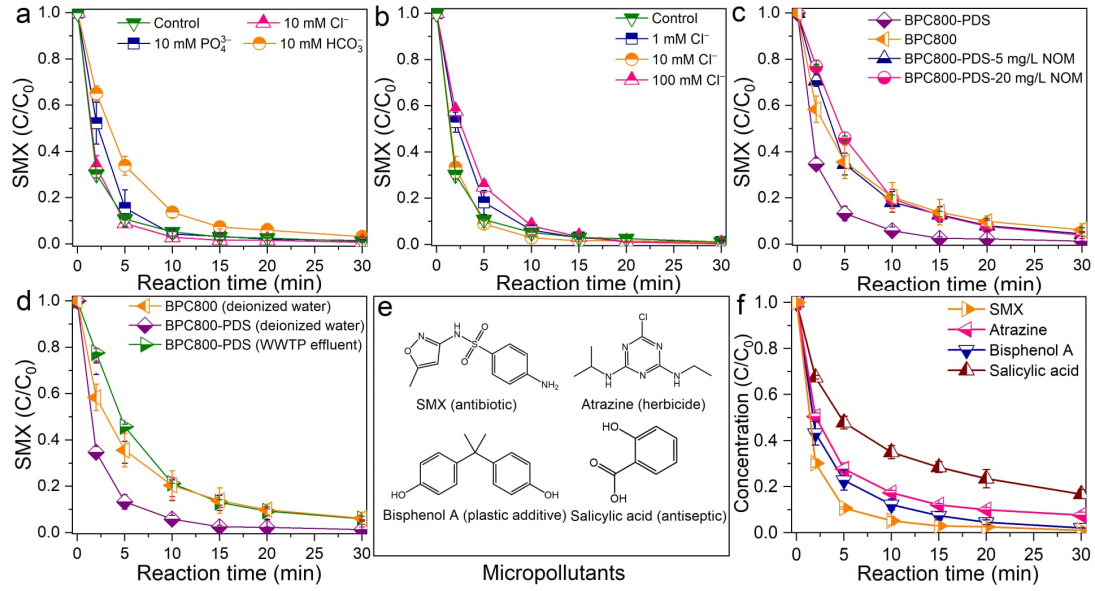

Figure 9. Effects of (a) common anions, (b) different levels of Cl^-, (c) NOMs, and (d) real water matrices on the removal of SMX by BPC800–PDS; (e) a list of micropollutants and (f) removal of these pollutants by BPC800–PDS. Conditions: [SMX] = 5 mg/L, (f) [atrazine] = [bisphenol A] = [salicylic acid] = 5 mg/L, [PDS] = 0.5 mM, [BPC800] = 50 mg/L, and pH = 3.0.

The inorganic anions in aquatic environments could act as radical scavengers in AOPs because of their high reaction rates with free radicals [61]. Although both $^{\cdot}OH_s$ and

$SO_{4,s}^{\cdot-}$ are currently poorly understood, some previous reports have shown that these oxidizing species are more selective than their free counterparts [37, 62]. To evaluate the practical applicability of BPC800–PDS, the catalytic removal of SMX in the presence of different anions was investigated. As shown in Fig. 9a, anions including chloride ions (Cl^-) and phosphate ions (PO_4^{3-}) up to 10 mM had no obvious scavenging effect on the removal of SMX. The presence of bicarbonate ions (HCO_3^-/CO_3^{2-}) slightly reduced the removal kinetics of SMX in the first 10 min, but their influence on the overall removal rate of SMX was negligible. A similar negligible effect was noticed when the concentration of Cl^- was further increased to 100 mM (Fig. 9b). The absence of an obvious inhibitory effect from these common anions indicates that the BPC800–PDS system has a high selectivity.

In addition to these anions, the effect of NOMs was also explored. Fig. 9c shows a decrease in the removal kinetics of SMX when NOMs (5, 10 mg/L) were added to the catalytic system, which was probably related to the competitive adsorption of NOMs. However, an overall removal rate up to 93.4%–95.2% was still achieved by BPC800–PDS in the presence of either 5 or 10 mg/L NOMs. Efficient removal of SMX was also obtained when the reaction media was changed from deionized water to the WWTP effluent (Fig. 9d). The TOC value (19.6 mg/L) (Table S2) shows that this effluent contained high levels of organic contaminants. The limited matrix effects consistently reveal that the catalytic combination of BPC800 with PDS had great stability and tolerance in the removal of SMX from real water samples.

A list of compounds other than SMX including salicylic acid, atrazine, and bisphenol A was selected and used to test the reactivity of BPC800–PDS (Fig. 9e). These

substances have wide applications (e.g., herbicide and plastic additive) and are representative of micropollutants. The pK_a values of these pollutants vary widely (Table S1), and thus they were expected to be present with different charges at pH 3.0. Fig. 9f shows that the overall removal rates of 83.2%, 92.3%, and 98.1% were achieved for salicylic acid, atrazine, and bisphenol A, respectively, after reaction for 30 min. The removal of the latter two contaminants by BPC800–PDS was very close to that of SMX, which suggests that this catalytic oxidation had high reactivity in the decontamination of micropollutants. The relatively slower kinetics in the removal of salicylic acid was probably because of its much greater initial molar concentration (36.2 μM) over other substances (19.7–23.2 μM).

4. Conclusions

In summary, a series of biomass-derived highly porous carbon materials were synthesized and used to catalytically remove representative micropollutants via the activation of PDS. Among them, the combination of BPC800 with PDS had the best performance for SMX removal. BPC800–PDS oxidation had a wide range of pH values from 3.0 to 9.0. Although both adsorption and oxidation contributed to the removal of SMX by BPC800–PDS, catalytic oxidation was the major removing mechanism. During the catalytic oxidation, free radicals and BPC800-mediated IET were not involved. Rather, BPC800 was found to form a complex with PDS ([BPC–PDS]*), and DET occurred in the complex, generating $SO_{4,s}^{\cdot-}$ and $^{\cdot}OH_s$ as the primary oxidizing species. The surface-bound state of radicals was evidenced by fluorescence microscopy. Four pathways were proposed for the degradation of SMX by these radicals. Common water constituents including Cl^-, PO_4^{3-}, HCO_3^-/CO_3^{2-}, and NOM had no obvious influence on the degradation of SMX by BPC800–PDS. Only a slight matrix effect was

observed when the degradation tests were performed in the WWTP effluent, which demonstrates the great potential of BPC800–PDS oxidation for practical water remediation. Although we preliminarily show the selectivity of BPC800–PDS oxidation in this study, the nature of surface-bound radicals and their interactions with catalyst surfaces remain largely unclear and require further study.

Declaration of Competing Interest

The authors declare that they have no known competing financial interests or personal relationships that could have appeared to influence the work reported in this paper.

Acknowledgements

This study was funded by the National Natural Science Foundation of China (52000080 and 42077340) and Guangdong Basic and Applied Basic Research Foundation (2019A1515110988 and 2019A1515110131). The authors gratefully acknowledge the support of 2022 Guangdong-Hong Kong-Macao Greater Bay Area Exchange Programs of SCNU.

References

[1] Q.Q. Zhang, G.G. Ying, C.G. Pan, Y.S. Liu, J.L. Zhao, Comprehensive evaluation of antibiotics emission and fate in the river basins of China: Source analysis, multimedia modeling, and linkage to bacterial resistance, Environmental Science & Technology, 49 (2015) 6772-6782.

[2] M. Bilal, M. Adeel, T. Rasheed, Y. Zhao, H.M.N. Iqbal, Emerging contaminants of high concern and their enzyme-assisted biodegradation - A review, Environment International, 124 (2019) 336-353.

[3] K.Z. Huang, H. Zhang, Direct electron-transfer-based peroxymonosulfate activation by iron-doped manganese oxide (delta-MnO_2) and the development of galvanic oxidation processes (GOPs), Environmental Science & Technology, 53 (2019) 12610-12620.

[4] A.B. Ross, P. Neta, Rate constants for reactions of inorganic radicals in aqueous solution, US Department of Commerce, National Bureau of Standards Washington D. C, 1979.

[5] X.Y. Yu, Critical evaluation of rate constants and equilibrium constants of hydrogen peroxide photolysis in acidic aqueous solutions containing chloride ions, Journal of Physical and Chemical Reference Data, 33 (2004) 747-763.

[6] G.V. Buxton, C.L. Greenstock, W.P. Helman, A.B. Ross, Critical review of rate constants for reactions of hydrated electrons, hydrogen atoms and hydroxyl radicals ($\cdot OH/\cdot O^-$) in aqueous solution, Journal of Physical and Chemical Reference Data, 17 (1988) 513-886.

[7] P.L. Brezonik, J. Fulkerson-Brekken, Nitrate-induced photolysis in natural waters: Controls on concentrations of hydroxyl radical photo-intermediates by natural scavenging agents, Environmental Science & Technology, 32 (1998) 3004-3010.

[8] L. Zhou, M. Sleiman, C. Ferronato, J.-M. Chovelon, C. Richard, Reactivity of sulfate radicals with natural organic matters, Environmental Chemistry Letters, 15 (2017) 733-737.

[9] Z. Li, M. Li, Z. Zhang, P. Li, Y. Zang, X. Liu, Antibiotics in aquatic environments of China: A review and meta-analysis, Ecotoxicology and Environmental Safety, 199 (2020) 110668.

[10] Z. Yang, J. Qian, A. Yu, B. Pan, Singlet oxygen mediated iron-based Fenton-like catalysis under nanoconfinement, Proceedings of the National Academy of Sciences,

116 (2019) 6659-6664.
[11] Y. Zhou, J. Jiang, Y. Gao, J. Ma, S.Y. Pang, J. Li, X.T. Lu, L.P. Yuan, Activation of peroxymonosulfate by benzoquinone: A novel nonradical oxidation process, Environmental Science & Technology, 49 (2015) 12941-12950.
[12] Z. Yang, J. Qian, C. Shan, H. Li, Y. Yin, B. Pan, Toward selective oxidation of contaminants in aqueous systems, Environmental Science & Technology, 55 (2021) 14494-14514.
[13] S. Wacławek, H.V. Lutze, K. Grübel, V.V.T. Padil, M. Černík, D.D. Dionysiou, Chemistry of persulfates in water and wastewater treatment: A review, Chemical Engineering Journal, 330 (2017) 44-62.
[14] Y. Zong, X. Guan, J. Xu, Y. Feng, Y. Mao, L. Xu, H. Chu, D. Wu, Unraveling the overlooked involvement of high-valent cobalt-oxo species generated from the cobalt(II)-activated peroxymonosulfate process, Environmental Science & Technology, 54 (2020) 16231-16239.
[15] N. Chen, G. Fang, C. Zhu, S. Wu, G. Liu, D.D. Dionysiou, X. Wang, J. Gao, D. Zhou, Surface-bound radical control rapid organic contaminant degradation through peroxymonosulfate activation by reduced Fe-bearing smectite clays, Journal of Hazardous Materials, 389 (2020) 121819.
[16] E.T. Yun, J.H. Lee, J. Kim, H.D. Park, J. Lee, Identifying the nonradical mechanism in the peroxymonosulfate activation process: Singlet oxygenation versus mediated electron transfer, Environmental Science & Technology, 52 (2018) 7032-7042.
[17] P.H. Shao, J.Y. Tian, F. Yang, X.G. Duan, S.S. Gao, W.X. Shi, X.B. Luo, F.Y. Cui, S.L. Luo, S.B. Wang, Identification and regulation of active sites on nanodiamonds: Establishing a highly efficient catalytic system for oxidation of organic contaminants, Advanced Functional Materials., 28 (2018) 8.
[18] C.H. Chu, J. Yang, D.H. Huang, J.F. Li, A.Q. Wang, P.J.J. Alvarez, J.H. Kim, Cooperative pollutant adsorption and persulfate-driven oxidation on hierarchically ordered porous carbon, Environmental Science & Technology, 53 (2019) 10352-10360.
[19] S. Zhu, C. Jin, X. Duan, S. Wang, S.-H. Ho, Nonradical oxidation in persulfate activation by graphene-like nanosheets (GNS): Differentiating the contributions of singlet oxygen ($^1O_2$) and sorption-dependent electron transfer, Chemical Engineering Journal, 393 (2020) 124725.

[20] H.Z. Wang, W.Q. Guo, B.H. Liu, Q.L. Wu, H.C. Luo, Q. Zhao, Q.S. Si, F. Sseguya, N.Q. Ren, Edge-nitrogenated biochar for efficient peroxydisulfate activation: An electron transfer mechanism, Water Research, 160 (2019) 405-414.
[21] P. Sun, H. Liu, M. Feng, Z. Zhai, Y. Fang, X. Zhang, V.K. Sharma, Strategic combination of N-doped graphene and g-C_3N_4: Efficient catalytic peroxymonosulfate-based oxidation of organic pollutants by non-radical-dominated processes, Applied Catalysis B: Environmental, 272 (2020) 119005.
[22] Y. Hu, D. Chen, R. Zhang, Y. Ding, Z. Ren, M. Fu, X. Cao, G. Zeng, Singlet oxygen-dominated activation of peroxymonosulfate by passion fruit shell derived biochar for catalytic degradation of tetracycline through a non-radical oxidation pathway, Journal of Hazardous Materials, 419 (2021) 126495.
[23] Y. Feng, Y. Li, G.G. Ying, Micro-interface electron transfer oxidation based on persulfate activation, Progress in Chemistry, 33 (2021) 2138-2149.
[24] H. Lee, H.-i. Kim, S. Weon, W. Choi, Y.S. Hwang, J. Seo, C. Lee, J.-H. Kim, Activation of persulfates by graphitized nanodiamonds for removal of organic compounds, Environmental Science & Technology, 50 (2016) 10134-10142.
[25] Y. Yang, G. Banerjee, G.W. Brudvig, J.H. Kim, J.J. Pignatello, Oxidation of organic compounds in water by unactivated peroxymonosulfate, Environmental Science & Technology, 52 (2018) 5911-5919.
[26] J. Chen, D. Zhang, H. Zhang, S. Ghosh, B. Pan, Fast and slow adsorption of carbamazepine on biochar as affected by carbon structure and mineral composition, Science of The Total Environment, 579 (2017) 598-605.
[27] S. Zhu, X. Huang, F. Ma, L. Wang, X. Duan, S. Wang, Catalytic removal of aqueous contaminants on N-doped graphitic biochars: Inherent roles of adsorption and nonradical mechanisms, Environmental Science & Technology, 52 (2018) 8649-8658.
[28] H. Wang, W. Guo, B. Liu, Q. Wu, H. Luo, Q. Zhao, Q. Si, F. Sseguya, N. Ren, Edge-nitrogenated biochar for efficient peroxydisulfate activation: An electron transfer mechanism, Water Research, 160 (2019) 405-414.
[29] X. Li, X. Huang, S. Xi, S. Miao, J. Ding, W. Cai, S. Liu, X. Yang, H. Yang, J. Gao, J. Wang, Y. Huang, T. Zhang, B. Liu, Single cobalt atoms anchored on porous N-doped graphene with dual reaction sites for efficient Fenton-like catalysis, Journal of American Chemical Society, 140 (2018) 12469-12475.
[30] Z. Sun, L. Zhao, C. Liu, Y. Zhen, J. Ma, Fast adsorption of BPA with high capacity

based on π-π electron donor-acceptor and hydrophobicity mechanism using an in-situ sp2 C dominant N-doped carbon, Chemical Engineering Journal, 381 (2020).
[31] C.H. Wang, W.C. Wen, H.C. Hsu, B.Y. Yao, High-capacitance KOH-activated nitrogen-containing porous carbon material from waste coffee grounds in supercapacitor, Advanced Powder Technology, 27 (2016) 1387-1395.
[32] C. Chu, J. Yang, D. Huang, J. Li, A. Wang, P.J.J. Alvarez, J.H. Kim, Cooperative pollutant adsorption and persulfate-driven oxidation on hierarchically ordered porous carbon, Environmental Science & Technology, 53 (2019) 10352-10360.
[33] S. Zhang, X. Quan, J.F. Zheng, D. Wang, Probing the interphase "HO zone" originated by carbon nanotube during catalytic ozonation, Water Research, 122 (2017) 86-95.
[34] C. Liang, C.F. Huang, N. Mohanty, R.M. Kurakalva, A rapid spectrophotometric determination of persulfate anion in ISCO, Chemosphere, 73 (2008) 1540-1543.
[35] C. Liang, Y.T. Lin, W.H. Shih, Treatment of trichloroethylene by adsorption and persulfate oxidation in batch studies, Industrial & Engineering Chemistry Research, 48 (2009) 8373-8380.
[36] A.L. Boreen, W.A. Arnold, K. McNeill, Photochemical fate of sulfa drugs in the aquatic environment: sulfa drugs containing five-membered heterocyclic groups, Environmental Science & Technology, 38 (2004) 3933-3940.
[37] J.M. Barazesh, C. Prasse, D.L. Sedlak, Electrochemical transformation of trace organic contaminants in the presence of halide and carbonate ions, Environmental Science & Technology, 50 (2016) 10143-10152.
[38] P. Chen, Y. Mu, Y. Chen, L. Tian, X.H. Jiang, J.P. Zou, S.L. Luo, Shifts of surface-bound •OH to homogeneous •OH in BDD electrochemical system via UV irradiation for enhanced degradation of hydrophilic aromatic compounds, Chemosphere, 291 (2022) 132817.
[39] H.R. Song, L.X. Yan, J. Jiang, J. Ma, Z.X. Zhang, J.M. Zhang, P.X. Liu, T. Yang, Electrochemical activation of persulfates at BDD anode: Radical or nonradical oxidation?, Water Research, 128 (2018) 393-401.
[40] J. He, Y. Xiao, J. Tang, H. Chen, H. Sun, Persulfate activation with sawdust biochar in aqueous solution by enhanced electron donor-transfer effect, Science of The Total Environment, 690 (2019) 768-777.
[41] J. Qin, L. Dai, P. Shi, J. Fan, Y. Min, Q. Xu, Rational design of efficient metal-

754 free catalysts for peroxymonosulfate activation: Selective degradation of organic
755 contaminants via a dual nonradical reaction pathway, Journal of Hazardous Materials,
756 398 (2020) 122808.
757 [42] J. Gonzalez, M. Torrent-Sucarrat, J.M. Anglada, The reactions of SO_3 with HO_2
758 radical and $H_2O\cdots HO_2$ radical complex. Theoretical study on the atmospheric
759 formation of HSO_5 and H_2SO_4, Physical Chemistry Chemical Physics, 12 (2010) 2116-
760 2125.
761 [43] T. Zhang, H. Zhu, J.-P. Croué, Production of sulfate radical from
762 peroxymonosulfate induced by a magnetically separable $CuFe_2O_4$ spinel in water:
763 efficiency, stability, and mechanism, Environmental Science & Technology, 47 (2013)
764 2784-2791.
765 [44] J. Liu, Z. Zhao, P. Shao, F. Cui, Activation of peroxymonosulfate with magnetic
766 Fe3O4–MnO2 core–shell nanocomposites for 4-chlorophenol degradation, Chemical
767 Engineering Journal, 262 (2015) 854-861.
768 [45] W. Ren, L. Xiong, X. Yuan, Z. Yu, H. Zhang, X. Duan, S. Wang, Activation of
769 peroxydisulfate on carbon nanotubes: Electron-transfer mechanism, Environmental
770 Science & Technology, 53 (2019) 14595-14603.
771 [46] M.M. Mian, G. Liu, B. Fu, Y. Song, Facile synthesis of sludge-derived MnOx-N-
772 biochar as an efficient catalyst for peroxymonosulfate activation, Applied Catalysis B:
773 Environmental, 255 (2019) 117765.
774 [47] G. Nardi, I. Manet, S. Monti, M.A. Miranda, V. Lhiaubet-Vallet, Scope and
775 limitations of the TEMPO/EPR method for singlet oxygen detection: the misleading
776 role of electron transfer, Free Radical Biology and Medicine, 77 (2014) 64-70.
777 [48] S. Zhang, X. Quan, J.F. Zheng, D. Wang, Probing the interphase "HO zone"
778 originated by carbon nanotube during catalytic ozonation, Water Research, 122 (2017)
779 86-95.
780 [49] S. Cai, Q. Zhang, Z. Wang, S. Hua, D. Ding, T. Cai, R. Zhang, Pyrrolic N-rich
781 biochar without exogenous nitrogen doping as a functional material for bisphenol A
782 removal: Performance and mechanism, Applied Catalysis B: Environmental, 291
783 (2021).
784 [50] W. Ren, L. Xiong, G. Nie, H. Zhang, X. Duan, S. Wang, Insights into the electron-
785 transfer regime of peroxydisulfate activation on carbon nanotubes: The Role of oxygen
786 functional groups, Environmental Science & Technology, 54 (2019) 1267-1275.

[51] W. McElroy, S. Waygood, Kinetics of the reactions of the SO_4^- radical with SO_4^-, $S_2O_8^{2-}$, H_2O and Fe^{2+}, Journal of the Chemical Society, Faraday Transactions, 86 (1990) 2557-2564.

[52] Y. Yang, X. Lu, J. Jiang, J. Ma, G. Liu, Y. Cao, W. Liu, J. Li, S. Pang, X. Kong, C. Luo, Degradation of sulfamethoxazole by UV, UV/H_2O_2 and UV/persulfate (PDS): Formation of oxidation products and effect of bicarbonate, Water Research, 118 (2017) 196-207.

[53] M. Abellán, W. Gebhardt, H.F. Schröder, Detection and identification of degradation products of sulfamethoxazole by means of LC/MS and− MSn after ozone treatment, Water Science and Technology, 58 (2008) 1803-1812.

[54] Y. Ji, Y. Fan, K. Liu, D. Kong, J. Lu, Thermo activated persulfate oxidation of antibiotic sulfamethoxazole and structurally related compounds, Water Research, 87 (2015) 1-9.

[55] S. Wang, W. Xu, J. Wu, Q. Gong, P. Xie, Improved sulfamethoxazole degradation by the addition of MoS_2 into the Fe^{2+}/peroxymonosulfate process, Separation and Purification Technology, 235 (2020).

[56] J. Du, W. Guo, D. Che, N. Ren, Weak magnetic field for enhanced oxidation of sulfamethoxazole by Fe^0/H_2O_2 and Fe^0/persulfate: Performance, mechanisms, and degradation pathways, Chemical Engineering Journal, 351 (2018) 532-539.

[57] L. Hu, P.M. Flanders, P.L. Miller, T.J. Strathmann, Oxidation of sulfamethoxazole and related antimicrobial agents by TiO_2 photocatalysis, Water Research, 41 (2007) 2612-2626.

[58] C. Guan, J. Jiang, S. Pang, J. Ma, X. Chen, T.T. Lim, Nonradical transformation of sulfamethoxazole by carbon nanotube activated peroxydisulfate: Kinetics, mechanism and product toxicity, Chemical Engineering Journal, 378 (2019).

[59] J. Yan, J. Li, J. Peng, H. Zhang, Y. Zhang, B. Lai, Efficient degradation of sulfamethoxazole by the CuO@Al_2O_3 (EPC) coupled PMS system: Optimization, degradation pathways and toxicity evaluation, Chemical Engineering Journal, 359 (2019) 1097-1110.

[60] R. Guo, Y. Wang, J. Li, X. Cheng, D.D. Dionysiou, Sulfamethoxazole degradation by visible light assisted peroxymonosulfate process based on nanohybrid manganese dioxide incorporating ferric oxide, Applied Catalysis B: Environmental, 278 (2020).

[61] H.V. Lutze, N. Kerlin, T.C. Schmidt, Sulfate radical-based water treatment in

820 presence of chloride: formation of chlorate, inter-conversion of sulfate radicals into
821 hydroxyl radicals and influence of bicarbonate, Water Research, 72 (2015) 349-360.
822 [62] Y. Feng, W. Qing, L. Kong, H. Li, D. Wu, Y. Fan, P.H. Lee, K. Shih, Factors and
823 mechanisms that influence the reactivity of trivalent copper: A novel oxidant for
824 selective degradation of antibiotics, Water Research, 149 (2019) 1-8.

825